JACS
JOURNAL OF THE AMERICAN CHEMICAL SOCIETY
Article
pubs.acs.org/JACS

Solar Cell Efficiency, Self-Assembly, and Dipole−Dipole Interactions of Isomorphic Narrow-Band-Gap Molecules

Christopher J. Takacs,[#] Yanming Sun,[#] Gregory C. Welch,[#] Louis A. Perez,[#] Xiaofeng Liu, Wen Wen, Guillermo C. Bazan,* and Alan J. Heeger*

Center for Polymers and Organic Solids, Departments of Chemistry & Biochemistry and Materials, University of California, Santa Barbara, California 93106, United States

Supporting Information

ABSTRACT: We examine the correlations of the dipole moment and conformational stability to the self-assembly and solar cell performance within a series of isomorphic, solution-processable molecules. These charge-transfer chromophores are described by a D^1-A-D-A-D^1 structure comprising electron-rich 2-hexylbithiophene and 3,3′-di-2-ethylhexylsilylene-2,2′-bithiophene moieties as the donor units D^1 and D, respectively. The building blocks 2,1,3-benzothiadiazole (BT) and [1,2,5]thiadiazolo[3,4-*c*]pyridine (PT) were used as the electron-deficient acceptor units A. Using a combination of UV−visible spectroscopy, field-effect transistors, solar cell devices, grazing incident wide-angle X-ray scattering, and transmission electron microscopy, three PT-containing compounds (**1**−**3**) with varying regiochemistry and symmetry, together with the BT-based compound 5,5′-bis{(4-(7-hexylthiophen-2-yl)thiophen-2-yl)-[1,2,5]thiadiazolobenzene}-3,3′-di-2-ethylhexylsilylene-2,2′-bithiophene (**4**), are compared and contrasted in solution, in thin films, and as blends with the electron acceptor [6,6]-phenyl-C_{70}-butyric acid methyl ester. The molecules with symmetric orientations of the PT acceptor, **1** and **2**, yield highly ordered blended thin films. The best films, processed with the solvent additive 1,8-diiodooctane, show donor "crystallite" length scales on the order of 15−35 nm and photovoltaic power conversion efficiencies (PCEs) of 7.0 and 5.6%, respectively. Compound **3**, with an unsymmetrical orientation of PT heterocycles, shows subtle differences in the crystallization behavior and a best PCE of 3.2%. In contrast, blends of the BT-containing donor **4** are highly disordered and give PCEs below 0.2%. We speculate that the differences in self-assembly arise from the strong influence of the BT acceptor and its orientation on the net dipole moment and geometric description of the chromophore.

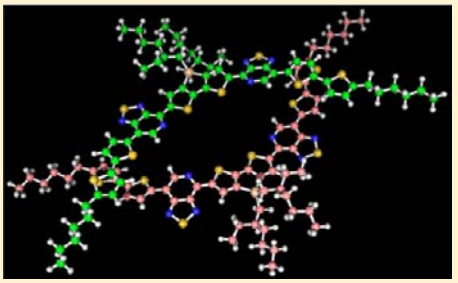

1. INTRODUCTION

Organic solar cells (OSCs) have the potential to act as cost-effective renewable energy sources, and thus have been the focus of considerable academic and industrial research.[1−10] The most studied active-layer structure is that of the bulk heterojunction (BHJ), which ideally consists of an interpenetrating network of electron-donor and electron-acceptor materials, either polymers or small molecules (or a combination of the two), and can be fabricated by solution casting or co-evaporation techniques.[11−24] Impressive power conversion efficiencies (PCEs) from 8.3% to 10.6% have been reported in the literature.[25−29] For OSCs constructed from vacuum-processed small molecules, PCEs of 6.4% and 10.7% have been reported for a single-layer BHJ solar cell and a multi-layer tandem solar cell, respectively.[30−32]

Solution-processed narrow-band-gap π-conjugated small molecules have received more attention recently for use as the donor component in fullerene-based BHJ solar cells.[33−41] Compared to their polymer counterparts, molecular donors have several advantages, including well-defined structures, higher purity, increased order, and reduced batch-to-batch variation.[42−45] In addition, the ability to process such materials via solution deposition enables the possibility of low cost roll-to-roll manufacturing.[46] The device performance of solution-processed small-molecule BHJ solar cells has steadily increased over the past few years, with PCE values reaching over 6% for single-layer BHJ solar cells.[41,47,48] In an effort to further increase the PCE of such solar cells, a detailed understanding of structure−property−function relationships of conjugated molecular donors is needed for designing improved materials.[49−52]

We recently reported on a new molecular donor, 5,5′-bis{(4-(7-hexylthiophen-2-yl)thiophen-2-yl)-[1,2,5]thiadiazolo[3,4-*c*]-pyridine}-3,3′-di-2-ethylhexylsilylene-2,2′-bithiophene (**1**), which is built upon the versatile [1,2,5]thiadiazolo[3,4-*c*]pyridine (PT) building block.[48,53−55] A PCE of 6.7% was achieved for solution-processed small-molecule organic photovoltaics (OPVs).[48] We have also reported on the molecular and solid-state thermal transitions of 12 related derivatives consisting of a D^1-PT-D-PT-D^1 architecture, where D and D^1 represent electron-rich aromatic moieties relative to PT, and we have established how structural variations influence frontier molecular orbital levels, solubility characteristics, and thermal transitions.[51]

Received: May 31, 2012
Published: September 6, 2012

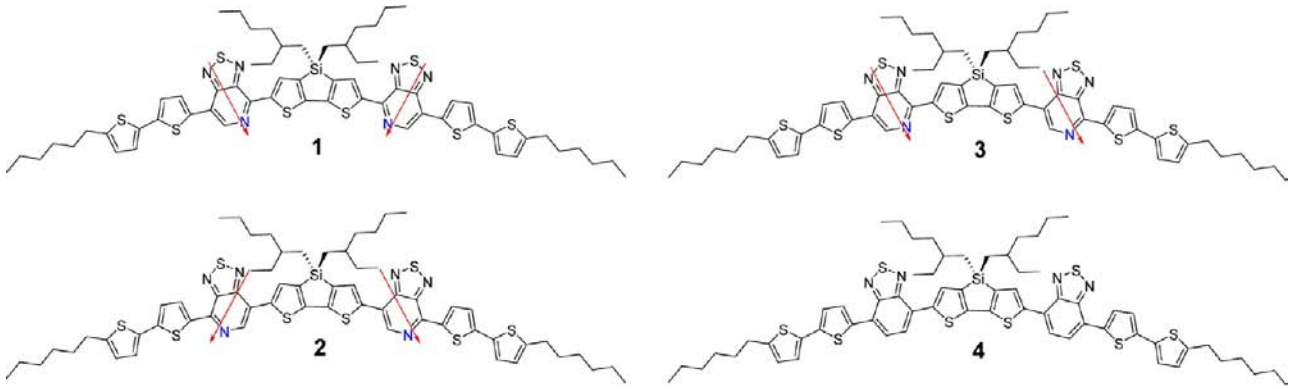

Figure 1. Molecular structures of compounds **1**, **2**, **3**, and **4**. Arrows are included to highlight pyridyl N-atom positions.

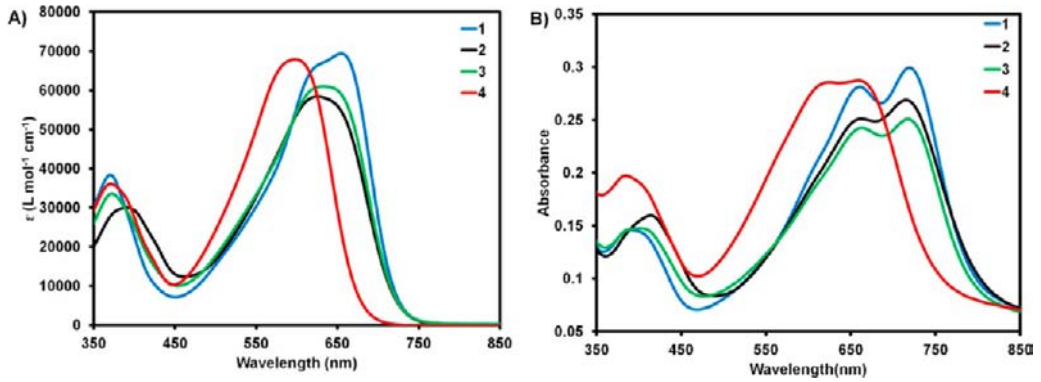

Figure 2. Optical absorption spectra of **1**–**4** in (A) CB solution and (B) thin films as cast from CB (10 mg/mL at 1200 rpm).

Table 1. Optical Absorption and Charge Transport Data for 1–4

	UV–vis								
	solution[a]				thin film[b]				
compd	ε (λ_{max}) (cm^{-1} M^{-1})	λ_{max} (nm)	λ_{onset} (nm)	E_{gap} (eV)	λ_{max} (nm)	λ_{onset} (nm)	E_{gap} (eV)	charge transport mobility (cm^{-2} V^{-1} s^{-1})	on/off ratio
1	69 583	657	735	1.69	720	825	1.50	0.20	8×10^4
2	58 221	630	730	1.70	712	825	1.50	0.07	6×10^5
3	61 434	632	730	1.70	715	815	1.52	0.05	1×10^5
4	68 146	595	690	1.80	663	785	1.58	0.01	6×10^4

[a]Solution spectra recorded in CB at room temperature in air. [b]Films cast from CB (10 mg/mL at 1200 rpm) onto quartz substrates in air.

In this contribution, we study the impact of the acceptor unit within the overall chromophore on the photovoltaic and morphological properties through a series of isomorphic small molecules related to **1**. Specifically, we study four compounds: three based on symmetrical and unsymmetrical regiochemistries of the PT acceptor and one based on the 2,1,3-benzothiadiazole (BT) acceptor. While the molecular structures of all the compounds are quite similar, one observes large differences in the PCE of OPV devices and the molecular ordering. The BT-containing compound shows large variation in the magnitude and direction of the molecular dipole as a function of molecular configuration. In comparison, the orientation of the PT acceptor unit has little influence on the net dipole moment. We speculate that this feature influences the thin-film self-assembly. The surprisingly significant impact of the acceptor sub-unit within the chromophore structure on bulk properties and device performance highlights the importance of synthetic design and active-layer processing conditions for realizing high-efficiency OSCs.

2. RESULTS AND DISCUSSION

2.1. Synthesis, Optical Characterization, and Thermal Characterization. The molecular structures of **1**–**4** are shown in Figure 1. Each compound has a general D^1-A-D-A-D^1 conjugated framework utilizing electron-rich 2-hexylbithiophene and 3,3′-di-2-ethylhexylsilylene-2,2′-bithiophene (DTS) moieties as the D^1 and D units, respectively. Synthetic details and spectroscopic characterization for **1**–**3** are reported elsewhere,[48,51,52] while that for **4** can be found in the Supporting Information. For **1**–**3**, the electron-deficient PT heterocycle is employed as the acceptor (A) unit with varying orientations of the pyridyl N-atom with respect to DTS, including proximal/proximal (**1**), distal/distal (**2**) and proximal/distal (**3**) regioisomers. For **4**, the BT acceptor was utilized as the A unit.

Solution UV–visible absorption spectra of **1**–**4** recorded in chlorobenzene (CB) are presented in Figure 2, with data summarized in Table 1. Absorption spectra of annealed thin films appear in the Supporting Information. Each compound exhibits broad optical absorption with distinct high- and low-

energy bands attributed to localized $\pi-\pi^*$ and internal charge-transfer transitions, respectively. The absorption maximum (λ_{max}) and onset of absorption (λ_{onset}) for **1**−**3** are similar, while the values for **4** show a blue-shift, attributed to the lower electron affinity of BT compared to the PT, consistent with related comparisons found in the literature.[53−56] Compounds **1** and **4** have slightly higher absorption coefficients in the low-energy band as compared to **2** and **3**. Given the high photon flux of the solar spectrum within this region (ca. 550−700 nm), the increased absorption coefficients are expected to lead to higher short-circuit currents in solar cell devices.

The transition from solution to the solid state in the form of thin films leads to a red-shift of the optical absorption spectra and the emergence of fine structure within the low-energy band, particularly for the PT-containing compounds. Such spectral changes are typically attributed to a planarization of the conjugated backbone and stronger $\pi-\pi$ interactions in the solid.[57,58] Optical band gaps were determined to be 1.50, 1.50, 1.52, and 1.58 eV for **1**, **2**, **3**, and **4**, respectively. Notably, **1**−**3** exhibit a more pronounced low-energy shoulder compared to **4**, from which we surmise a higher degree of disorder in the solid film. This notion is supported by X-ray diffraction experiments where neat films of **1**−**3** exhibit relatively more intense diffraction patterns than neat films of **4** (Supporting Information). The HOMO energy levels of **1**−**4** as thin films cast from CB were determined by ultraviolet photoelectron spectroscopy (UPS) and cyclic voltammetry (CV). The UPS values are shown in Figure 3 with additional details in the

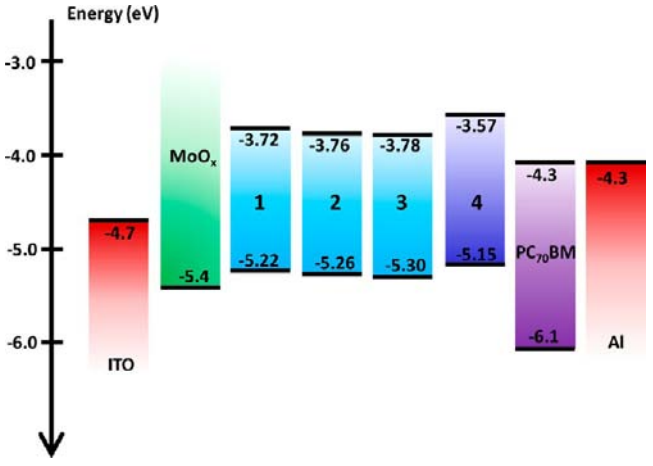

Figure 3. HOMO and LUMO energy levels of **1**−**4** (determined via UPS), $PC_{70}BM$, MoO_x hole transport layer, and Al cathode.

Supporting Information. In each case the HOMO energy levels are below −5.20 eV; thus, these should lead to differences in small-molecule−fullerene (HOMO−LUMO) energy gaps that translate into large open-circuit voltages (V_{oc}).[10]

Compound **4** exhibits a melting transition (T_m) at ∼122 °C as determined by differential scanning calorimetry (DSC) (Figure S6). This value is considerably lower than those observed for **1**−**3** ($T_m \approx$ 202−210 °C).[48,51,52] These results demonstrate the increased thermal stability imparted on the solid-state structure by PT, relative to BT.

2.2. Device Performance. Here we extend the device processing framework defined in our previous study of **1** and evaluate the performance of **2**−**4** under the same processing conditions. The pristine materials were studied using organic field-effect transistors and show hole mobilities of 0.20, 0.07, 0.05, and 0.01 $cm^2\ V^{-1}\ s^{-1}$ for **1**−**4**, respectively (Figure S8). Further details are provided in the Supporting Information. In BHJ films, although the mechanism is not yet fully understood, the solvent additive 1,8-diiodooctane (DIO) has previously been shown to optimize **1**:$PC_{70}BM$ devices, causing significant changes to the morphology and device performance.[48]

In the context of this study, the solvent additive becomes an important tool for evaluating the similarities and differences of **1**−**4**. Solar cell devices were fabricated using the conventional architecture of ITO/MoO_x/donor:$PC_{70}BM$/Al.[48,59] Current density−voltage ($J-V$) characteristics of solar cell devices based on **1**−**4** as a function of [DIO] under simulated AM 1.5 G irradiation (100 mW cm^{-2}) are shown in Figure 4. The incident photon conversion efficiency (IPCE) spectra are given in the Supporting Information (Figure S9). The short-circuit current (J_{sc}), V_{oc}, and fill-factor (FF) device data are tabulated in Table 2.

The best devices were based on **1** and **2**, the symmetric PT-containing materials, processed with the solvent additive. When processing with 0.25% v/v DIO solvent additive, the PCE based on **1**:$PC_{70}BM$ (**2**:$PC_{70}BM$) is 6.7% (5.6%) with J_{sc} = 14.4 mA cm^{-2} (12.7 mA cm^{-2}), FF = 59.3% (60%), and V_{oc} = 0.78 V (0.73 V). These devices both show high FFs suggesting good charge-transport properties. But the 50 mV lower V_{oc} and the 1.7 mA cm^{-2} lower J_{sc} combine to reduce the overall PCE more than a percent. As discussed earlier, the reduced J_{sc} of **2** relative to **1** is likely related to changes in the absorption spectrum; however, the origin of the lower V_{oc} is not currently understood. We note that 0.25% v/v DIO is not necessarily the optimum: further optimization of **1** shows that a best PCE of >7% with J_{sc} = 14.6 mA cm^{-2}, V_{oc} = 0.78 V, and FF = 62% can be achieved using a slightly higher [DIO] (0.27% v/v DIO, Figure S10). Increasing [DIO] beyond this nominal range quickly leads to a decrease in the PCE for both compounds. Incorporation of 1.0% v/v DIO decreased the PCE to less than 0.5% for both materials and, as we demonstrate later, this is likely due to large-scale phase separation of the donor. Thus, the symmetric PT-containing **1** and **2** show qualitatively similar trends suggesting relatively minor changes going from proximal/proximal to distal/distal orientation of the pyridyl N-atom.

The loss of molecular symmetry in **3** has two particularly interesting consequences for the solar cell devices (Figure 4C). First, while use of 0.25% v/v DIO solvent additive yields the best OPV performance for **3**:$PC_{70}BM$ solar cells (PCE = 3.2%), the overall efficiency is noticeably reduced compared to **1** and **2** under similar conditions. The low performance might be attributed to increased packing frustration from the reduced molecular symmetry giving rise to different interactions with $PC_{70}BM$ and different BHJ morphologies (*vide infra*). Second, at the highest tested concentration of 1.0% v/v DIO, BHJ films of **3**:$PC_{70}BM$ show the "best" PCE of 1.5%, as compared to 0.43% (0.26%) from **1**:$PC_{70}BM$ (**2**:$PC_{70}BM$) under the same conditions. The loss of molecular symmetry may self-limit large-scale aggregation in the thin film and widen the processing window. That this behavior differs from the symmetric compounds highlights how the molecular symmetry has a subtle effect on the device performance.

Quite significantly, despite the similarities in molecular properties, devices based on **4**:$PC_{70}BM$ did not show obvious photovoltaic behavior under these processing conditions. The addition of up to 1% v/v DIO solvent additive to the blend solutions has minimal impact on the device performance.

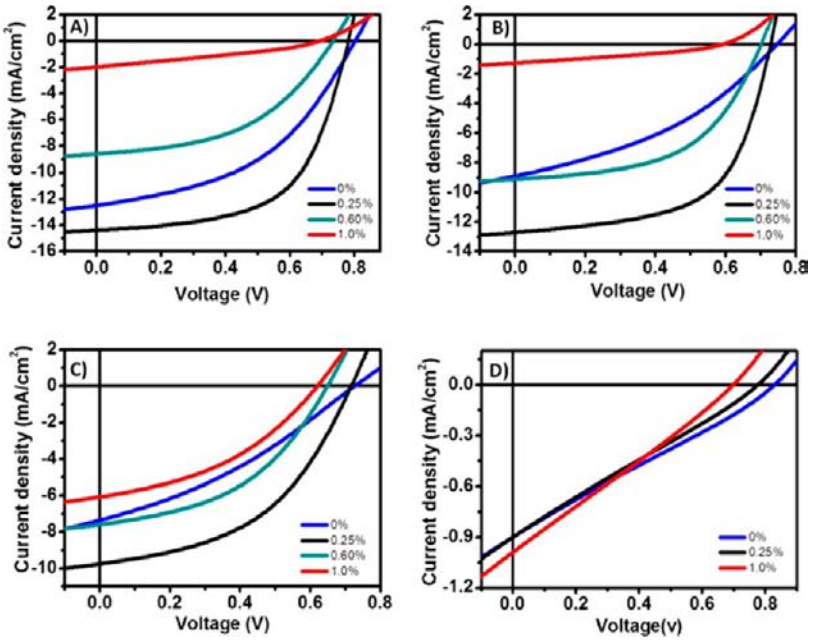

Figure 4. Current–voltage characteristics of small-molecule BHJ solar cells based on **1** (A), **2** (B), **3** (C), and **4** (D) blends (70:30 wt/wt) with $PC_{70}BM$ as a function of DIO content in mixed solutions (by volume). Panel (4) is taken from ref 48.

Table 2. Summary of Device Parameters of Small-Molecule BHJ Solar Cells Based on Small-Molecule:$PC_{70}BM$ Active Layers (4 wt % in CB Solvent with 70:30 Ratio) with Varying [DIO]

compd	DIO (% v/v)	V_{oc} (V)	J_{sc} (mA/cm^2)	FF (%)	PCE (%)
1[c]	0	0.80	12.5	45.2	4.52
	0.25	0.78	14.4	59.3	6.70
	0.6	0.74	9.2	47.5	3.20
	1	0.70	2.0	31.1	0.43
2	0	0.75	8.9	37.0	2.47
	0.25	0.73	12.7	60.0	5.56
	0.6	0.70	9.1	53.5	3.41
	1	0.60	1.3	33.3	0.26
3	0	0.73	7.4	33.1	1.78
	0.25	0.72	9.8	45.0	3.16
	0.6	0.65	7.6	44.5	2.20
	1	0.62	6.0	40.0	1.50
4	0	0.83	0.9	25.8	0.19
	0.25	0.78	0.9	25.4	0.18
	1	0.70	1.0	26.2	0.18

[c]Device data of **1** taken from ref 48.

Clearly, under these processing conditions molecule **4** and $PC_{70}BM$ are unable to self-assemble into suitable BHJ morphologies. We note that thermal annealing and incorporation of up to 1% v/v 1-chloronaphthalene, another common solvent additive used to improve device performance, did not improve the OPV performance. This low device performance highlights the importance of incorporating the pyridyl N-atom within the overall chromophore structure.

2.3. Morphological Characterization. The microstructure of the BHJ films was probed via grazing incidence wide-angle X-ray scattering (GIWAXS), high-resolution transmission electron microscopy (HR-TEM), and dark-field TEM. GIWAXS is a widely employed technique to determine structural ordering of donor/acceptor blend thin films.[60−62] HR-TEM and dark-field TEM are projection techniques that give complementary information about the spatial distribution of ordered donor material. As shown in our previous study, HR-TEM can directly image the donor lattice planes of ∼2 nm oriented in-plane.[48,63,64] The GIWAXS and HR-TEM images will be compared directly and the dark-field TEM results will be discussed near the end of this section. For **1**−**4**:$PC_{70}BM$ BHJ blends processed with 0.25% v/v DIO, the integrated intensities versus scattering wave vector, q, are shown in Figure 5, and the HR-TEM images are shown in Figure 6. For added clarity, the HR-TEM images have been overlaid with

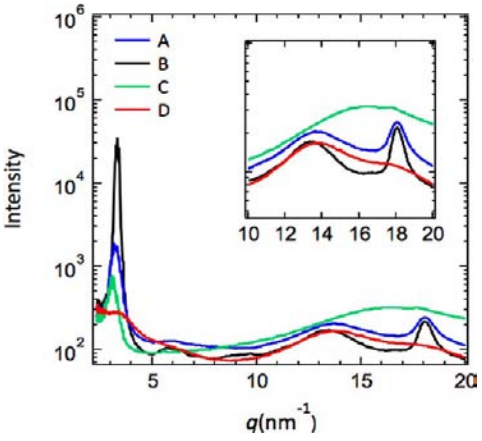

Figure 5. GIWAXS of small-molecule donor/fullerene blend films cast from CB on MoO_x/ITO substrates with 0.25% DIO additive: (A) **1**:$PC_{70}BM$, (B) **2**:$PC_{70}BM$, (C) **3**:$PC_{70}BM$, and (D) **4**:$PC_{70}BM$. The inset in the top right is a close-up of the region where $\pi-\pi$ stacking is expected. The scattering vector is defined as $q = 4\pi \sin(\theta)/\lambda$, where λ is the incident X-ray wavelength and θ is half the scattering angle. The 1D plot represents the azimuthally integrated intensity from the 2D detector.

dx.doi.org/10.1021/ja3050713 | J. Am. Chem. Soc. 2012, 134, 16597−16606

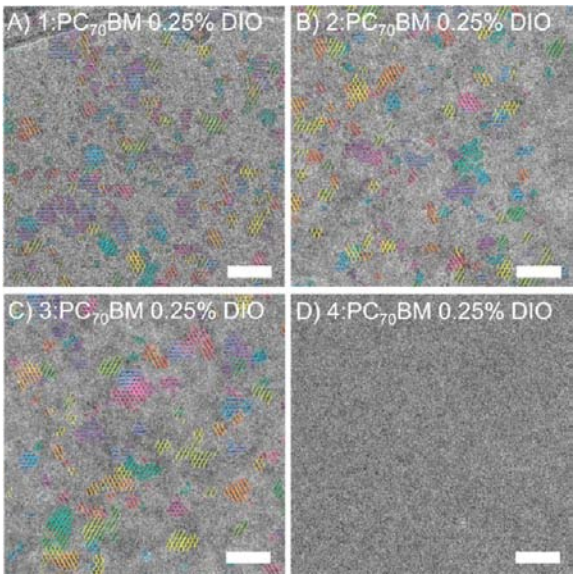

Figure 6. HR-TEM images of BHJ films processed with 0.25% v/v DIO: (A) **1**, (B) **2**, (C) **3**, and (D) **4**, all blends with $PC_{70}BM$ (70:30 wt/wt). Lattice planes of ∼2 nm are clearly resolvable in all films except for **4** and have been overlaid with colored lines to aid the reader. Additional diffraction contrast, mainly due to scattering of the donor around 18 nm^{-1}, is present in (B) and (C). All scale bars are 50 nm.

colored lines parallel to the observed lattice planes. Both symmetric PT-containing blend films of **1**:$PC_{70}BM$ and **2**:$PC_{70}BM$ display strong Bragg reflections at $q \approx 3$ and 18 nm^{-1} that indicate the presence of crystalline domains with similar packing structures. The degree of ordering of **1** and **2** is also presumed to be long range based on the observation of second- and third-order peaks centered at $q \approx 6$ and 9 nm^{-1} respectively. The reflection at $q \approx 18$ nm^{-1} is attributed to a $\pi-\pi$ stacking distance,[52] while the broad hump centered at $q \approx 13$ nm^{-1} is due to amorphous scattering.[65] The HR-TEM image of **1**:$PC_{70}BM$ (**2**:$PC_{70}BM$) in Figure 6A (Figure 6B) shows ordered donor regions of order 15−25 nm (20−30 nm) covering the film and the change in size is qualitatively consistent with the observed X-ray peak widths.

The **3**:$PC_{70}BM$ films exhibit reflections similar to those of **1** and **2** with $q \approx 3$ nm^{-1} along with larger crystallites (of order 25−50 nm) in the HR-TEM images (Figure 6C); however, the absence of higher order peaks and the broad peak extending from $q \approx 12$ to 20 nm^{-1} suggests a larger degree of disorder. This is consistent with the lower mobility observed in the transistor measurements and would contribute to the lower FF observed in the blend films. The proximal/distal positions of the pyridyl N-atom reduces the molecular symmetry and likely leads to increased packing frustration relative to BHJ blends of **1** and **2**. Thus, the X-ray scattering data and HR-TEM images demonstrate the presence of semi-crystalline or well-ordered microstructure for the PT acceptor moiety (**1**−**3**) when blended with $PC_{70}BM$. The highest PCE devices show ordered donor regions with length scales of 15−30 nm.

Of the four blends investigated, **4**:$PC_{70}BM$ films exhibits the lowest degree of order. The decreased amount of ordering is evident by the appearance of weak broad reflections at $q \approx 3$ and 18 nm^{-1} in Figure 5 and the complete absence of crystalline material in the HR-TEM image (Figure 6D). The lack of crystallinity and, presumably, phase separation within these thin films helps explain the low device performance.[40,41,52,66]

We used dark-field TEM imaging to examine the $q \approx 18$ nm^{-1} crystallite population. The results reveal a lateral organization approaching the micrometer scale in the blend films. Dark-field imaging spatially maps crystals *oriented in a specific direction*. This procedure is accomplished by inserting a small, circular aperture in the diffraction plane of the microscope, i.e., the back-focal plane of the objective lens, which subtends ∼50° of the ring corresponding to ∼18 nm^{-1}. Thus, the regions of the image that appear "bright" correspond to crystalline regions of the sample locally oriented such that they scatter electrons through the aperture. Dark-field images of **2**:$PC_{70}BM$ processed with 0.25% DIO are shown in Figure 7.

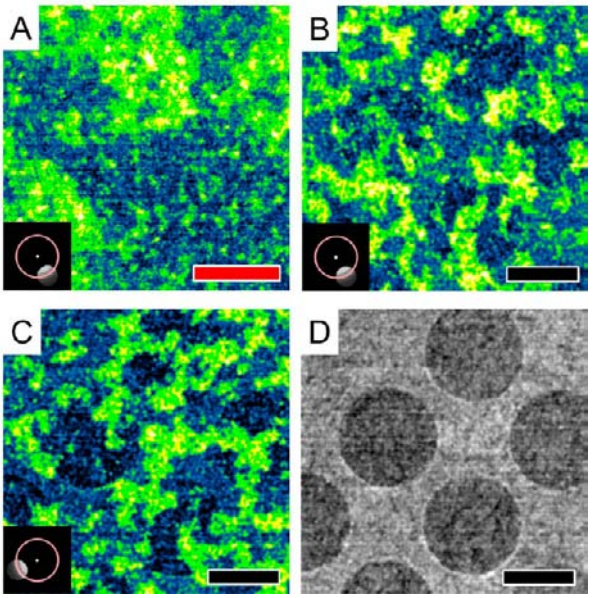

Figure 7. Dark-field images of **2**:$PC_{70}BM$ with 0.25% v/v DIO. (A) Both small crystals and large agglomerates of crystals. (B,C) After reducing the magnification to visualize the large agglomerates, two orthogonal in-plane crystallite orientations at a fixed position on the sample drawn from an image series covering the $q \approx 18$ nm^{-1} ring. The position of the circular aperture is shown in relation to the ring of the donor in the inset. The images show nearly complementary structure extending across the sample plane. (D) Nearly featureless image resulting from adding all of the dark-field images, except for the array of 2 μm holes of the C-Flat TEM grids. In order of increasing intensity, the image color scheme is black, blue, green, yellow, and white. The red and black scale bars are 200 nm and 1.5 μm, respectively.

The approximate location of the aperture in reciprocal-space appears in the inset. At magnifications similar to the HR-TEM images (Figure 7A), the **2**:$PC_{70}BM$ with 0.25% v/v DIO shows two distinct structures: a speckle-like structure we attribute to randomly distributed small crystals (of comparable size as observed in the HR-TEM images) and large, island-like agglomerates composed of small crystals having similar orientations. This later population is particularly interesting as it implies inter-crystallite ordering over length scales >100 nm. Similar order has been observed in electronically active polymeric materials, particularly those with high mobilities.[67,68] We observe similar results for blend films of **1** and **3** processed with and without the additive; however, no discernible order is observed for **4** blend films (Supporting Information).

dx.doi.org/10.1021/ja3050713 | *J. Am. Chem. Soc.* 2012, 134, 16597−16606

To illustrate the extent of these agglomerates, lower magnification dark-field images of **2**:$PC_{70}BM$ processed with 0.25% v/v DIO, ~6 μm per side, were acquired. Two orthogonal crystallite directions from the same sample area are shown in Figure 7B,C. These two images are part of a series covering the $q \approx 18$ nm^{-1} ring with an angular resolution of 15°. This pair highlights the large-scale structure and demonstrates nearly complementary coverage of the film, i.e., bright regions in one image are likely dark in the other. Furthermore, adding of all the images in the dark-field series results in a nearly homogeneous/featureless image (Figure 7D) showing nearly complete coverage of the film plane; however, the volume fraction of the film contributing to this population is unknown. The data were further reduced (details in the Supporting Information) into the effective director field shown in Figure 8. The short axis of the tic marks and their

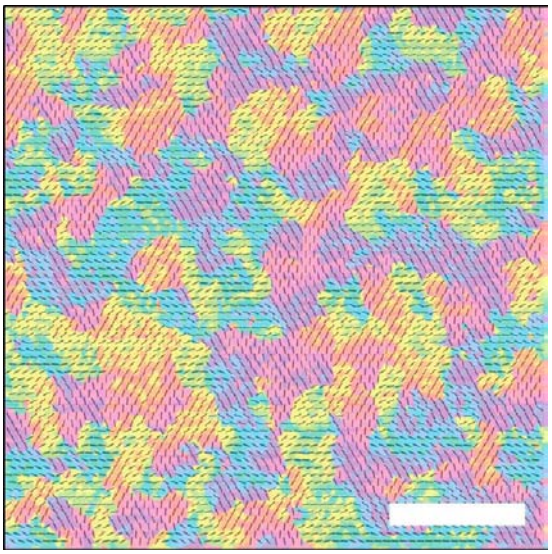

Figure 8. Map of the effective local director field reconstructed from a dark-field series with an angular resolution of 15°. The tic marks, drawn parallel to what we think is the long axis of the molecule, and color correspond to the local dominant direction. Domains approaching the micrometer scale are frequently observed throughout, along with many domains connected by smooth deformations of the director field. The scale bar is 1.5 μm.

surrounding color are drawn in the direction with the strongest intensity observed locally in the dark-field image series. We postulate that the long axis of the molecules corresponds with the long axis of the tic marks. Interestingly, not only is nearly micrometer-scale order observed within the high PCE blend film, but many of these regions are connected by smooth deformations of the director field like in a liquid crystal. The quantification and implications of this long-range order on the device performance will be the focus of future study.

At high [DIO], we observe a large increase in the donor domain size going from tens of nanometers to hundreds of nanometers. Figure 9 shows a comparison of HR-TEM images of **3**:$PC_{70}BM$ films processed with 0%, 0.25%, and 0.6% v/v DIO along with a dark-field image of the 0.6% v/v DIO blend film. For the high [DIO], the large increase in the crystallite size shown in the HR-TEM and dark-field images may reduce the efficiency of charge separation processes and reduce the total number of free charge-carriers generated in the blend film. Thus, these changes in morphology are likely linked to the

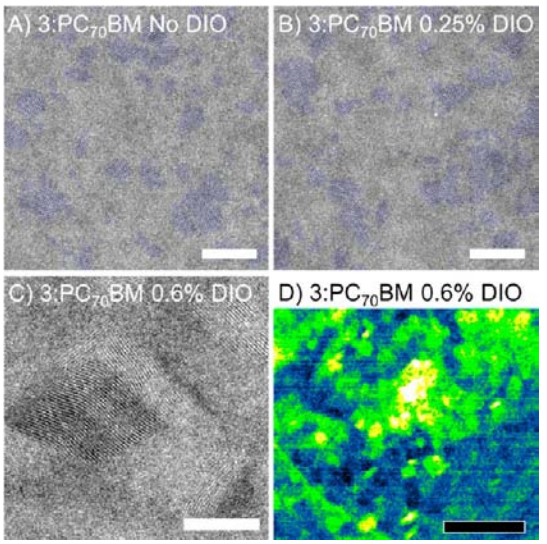

Figure 9. HR-TEM showing diffraction contrast and ~2 nm lattice planes of the donor phase of **3**:$PC_{70}BM$ (70:30 wt/wt) blended films: (A) processed from CB, (B) processed with 0.25% v/v DIO, (C) processed with 0.6% v/v DIO, and (D) expanded field of view of films processed with 0.6% v/v DIO using only diffraction contrast from large crystallites. The white (black) scale bar is 50 nm (200 nm). (Figures 6B and 7B show images of different spots from the same film.)

lower J_{sc} for **1**, **2**, and **3** BHJ blends as compared to the devices processed under the best conditions. Similar results at high [DIO] are observed in **1**:$PC_{70}BM$ films (Figure S13) and are expected to occur in **2**:$PC_{70}BM$ films.

It is reasonable to ask why the long-range order in the BHJ blends is readily observed in the dark-field images but not in the HR-TEM images. We again note that both techniques measure the 2D projection of the full 3D morphology, which means we can only guess as to the vertical location of the structures we observe. The $q \approx 18$ nm^{-1} and 3 nm^{-1} populations are likely probing, to some degree, different volumes within the film. Interestingly, the pristine thin films of **1** (i.e., without fullerene or additive) do show long-range, inter-crystallite order directly in the HR-TEM images (Supporting Information) along with similar structure in the dark-field images as observed in the blend. Thus, the addition of fullerene (and the additive) appears to changes the nucleation of the donor; however, some degree of the long-range order does persist in the film.

It is also worth noting that HR-TEM imaging of the high [DIO] samples is particularly sensitive to beam damage induced drift. Scanning transmission electron microscopy is also capable of resolving the lattice plans ($q \approx 3$ nm^{-1}) from large crystals (Figure S14) and is less affected by sample drift. The conceptual advantages of this method are discussed in the Supporting Information.

2.4. *Ab Initio* Calculations: Dipole Moments and Conformational Freedom. The morphological differences in Figures 5–7 between the PT- and BT-containing chromophores point to the acceptor unit playing a critical aspect in the self-assembly of the thin film. The equilibrium geometry and dipole moment of **1**–**4** were thus calculated using density functional theory (DFT) to a RB3LYP/6-311G(d,p) level of theory in the gas phase. The equilibrium structure of all compounds was found to adopt a similar bent-core shape reminiscent of "banana"-shaped liquid crystals.[69]

dx.doi.org/10.1021/ja3050713 | J. Am. Chem. Soc. 2012, 134, 16597–16606

The optimized banana shape of **1** (without the hexyl and ethylhexyl solubilizing groups) and the direction of the dipole moment (+0.4 D) are shown in Figure 10A. The self-assembly

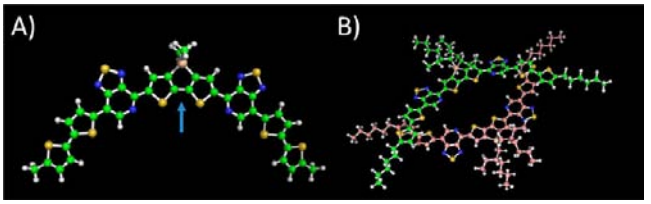

Figure 10. (A) Ground-state configuration from DFT optimization of **1**. The solubilizing groups have been omitted for clarity, and the blue arrow signifies the direction of the dipole moment. (B) Dimer self-assembly with partial cancelation of the dipole moment including the side groups.

of these bent compounds is likely driven, in some part, by the local electrostatics environment. At the simplest level, they will tend to minimize the net dipole moment. A cartoon representation of a dimer where both molecules of **1** are in the banana configuration is shown in Figure 8B. This ansatz has the individual dipole moments of the molecules antiparallel, as would be anticipated to lower the overall energy.

For packing in the solid state, it is useful to consider the structure, energy, and electrostatics of the low-energy conformers and how these may affect the self-assembly process.[70−72] We restrict our attention to **1** and **4**, the best- and worst-performing compounds, respectively. Figure 11 shows the dipole vector for six conformations. Optimized structures, tabulated energies, and dipole moments appear in the Supporting Information.

Compound **4**, the BT-containing compound, shows less energy difference between the different conformers and larger changes in both the magnitude and direction of the dipole moment. The banana configuration is also the lowest energy configuration, and the dipole moment is −1.8 D. We find both the "zigzag" and "twisted bithiophene" conformations are about 1 kT higher in energy than the banana conformation, suggesting that a relatively large population of these conformations will be present. As depicted in Figure 11, the zigzag conformation shows a pronounced reorientation of the dipole moment due to the flip of the BT unit. Looking at the symmetric "banana-with-flipped-bithiophenes" and "inverted banana" conformations, both separated by about 2 kT in energy from the banana conformation, the dipole moment is −0.5 and +3.7 D, respectively. The "banana-with-flipped-acceptors" configuration is about 5 kT in energy and the dipole moment is +2.7 D. The change in the dipole orientation may correlate with the poor self-assembly observed in the thin film. For example, to form a dimer with a combination of the banana and banana-with-flipped-acceptors configurations similar to the representation in Figure 10B, the dipole moments of the molecules will be forced in the same direction, raising the energy of the system. Nesting these molecules, i.e., anti-parallel alignment of the dipoles, to lower the net energy is likely prohibitive due to the steric hindrance of the ethylhexyl solubilizing groups. Thus, based on the broad statistical distribution of conformers and the potentially costly dipole−dipole interactions, the self-assembly rate could be low. Such reasoning is consistent with the low degree of observed order in the thin film.

In **1**, the introduction of the pyridyl N-atoms into the acceptor reduces the variation of the dipole moment as the molecular conformation is changed. Furthermore, the structure appears to be stabilized by an additional nonbonding interaction between the pyridyl N-atom and its nearest neighboring sulfur heteroatom. Borrowing the term "conformational lock" from Huang et al., this stabilizing interaction changes the conformer energy distribution.[73] The twisted

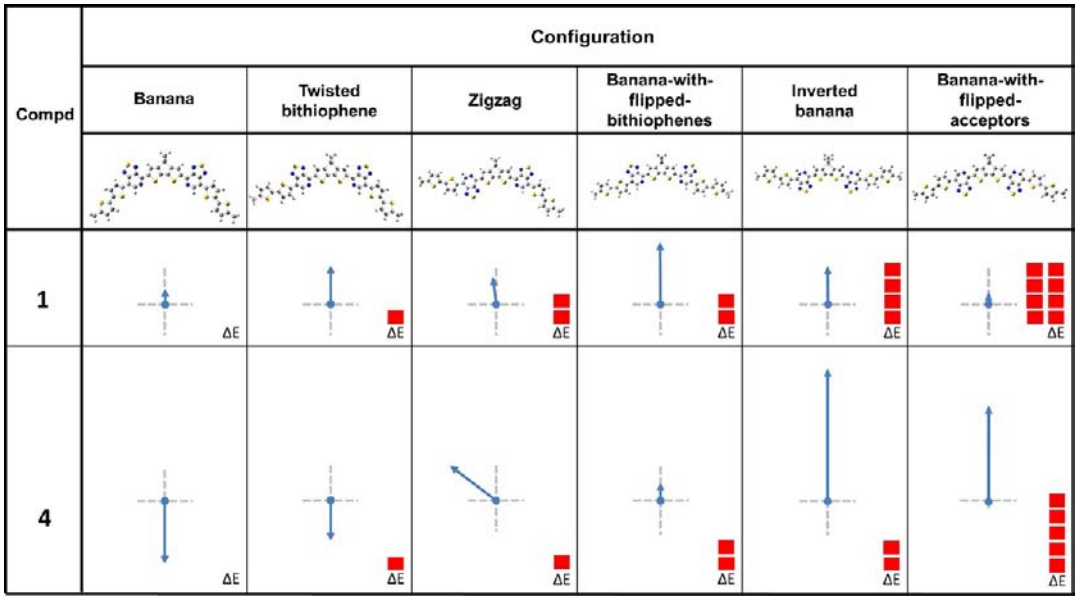

Figure 11. Energy relative to the "banana" configuration and dipole moment for six conformations of **1** and **4** as computed by RB3LYP/6-311G(d,p) in the gas phase. The blue arrow shows the magnitude and direction of the dipole moment. For scale, the dipole moment of **1** (**4**) in the banana configuration is +0.5 (−1.7) Debye and each red square represents ∼1 kT of energy above the banana configuration. Compound **4**, the BT-containing compound, shows larger changes of the dipole moment along with more low-energy conformers than **1**. The larger conformer distribution and dipole moment variations suggest self-assembly will be inhibited in **4**.

dx.doi.org/10.1021/ja3050713 | J. Am. Chem. Soc. 2012, 134, 16597−16606

bithiophene conformation is still the lowest in energy, costing ∼1 kT, but breaking the conformational lock makes the zigzag configuration more energetically costly, about 2 kT above the banana shape. The dipole moment for the twisted bithiophene and zigzag configurations changes to +1.1 and +0.8 D, respectively, and are approximately in the same direction as the banana configuration (+0.4 D). The symmetric banana-with-flipped-bithiophenes, inverted banana, and banana-with-flipped-acceptors configurations are now separated by ∼2, 4, and 8 kT, with dipole moments of +1.7, +1.1, and +0.1 D, respectively. In contrast to **4**, all of the considered configurations have the dipole moments in the same general direction allowing for antiparallel alignment and lowering of the overall energy. From the narrower distribution of conformers and their favorable dipole−dipole interactions, it is reasonable to expect better self-assembly in thin films of **1**. Of course, the formation of the BHJ morphology is a complex issue. We expect interactions with the solvent, solvent additive, and fullerene to influence self-assembly, e.g., changing the formation time scale, screening of the interactions, changing the accessible conformations, inducing disorder, etc. Still, this hypothesis correlates well with the experimental observations and may prove to be a useful consideration in the design of new small-molecule materials.

3. CONCLUSION

The optical, electronic, and morphological properties of four related D^1-A-D-A-D^1-type small molecules have been investigated. Specifically, we have compared BT- and PT-based small molecules to understand the significance and effect of pyridyl N-atom incorporation into the acceptor unit along with the role of the regiochemistry on the molecular and BHJ properties.

Differences in the blend films became evident when evaluating the photovoltaic and morphological characteristics as a function of the solvent additive DIO from 0% to 1% v/v. We observe that the [DIO] can change both the molecular order and domain sizes and is a useful method for amplifying differences between the compounds. The exact mechanism by which the DIO changes the film is still under debate; however, we do suspect that part of its role is to change the nucleation of the donor along with changing the time scale of the film formation process. The BT-based small molecule exhibits no observable crystalline nanostructures or signs of phase separation when blended with $PC_{70}BM$ and a poor photovoltaic performance (0.18%) under all tested processing conditions. In contrast, the PT regiochemistry within the molecular backbone was found to be important to the molecular self-assembly and solar cell device performance. The proximal/proximal (distal/distal) position of the pyridyl N-atoms in **1** (**2**) is symmetric about the central DTS donor unit and the blend films show the formation of a highly ordered nanomorphology when blended with $PC_{70}BM$, giving PCEs upward of 7% (5.6%). Near the optimal [DIO], **1** (**2**) showed crystallites with length scales of 15−25 nm (20−30 nm) in the blend films. However, at high [DIO] the crystallites size increases (>100 nm) and the PCE is <0.5%. Changing the position of the pyridyl N-atoms to the less symmetric distal/proximal configuration relative to the central DTS donor unit (**3**) reduces the ability of the material to self-assemble in the BHJ film. Both the short-circuit current and fill-factor are lower yielding a best PCE of 3.2%. Interestingly, the PCE is still 1.5% at the highest [DIO], significantly better than for **1** and **2**, suggesting the loss of molecular symmetry may prevent large-scale aggregation of the donor.

Compounds **1**−**3** also show a peculiar inter-crystallite ordering where the direction of small, neighboring crystallites are highly correlated. These correlations can approach the micrometer scale even in a high-performance blend film with a structure similar to a liquid crystal. This structure may have important effects on the local transport properties and device properties. For example, the misorientation between neighboring crystallites may be reduced which could allow for better local transport, lower rates of recombination, etc. Our current thinking is that the influence of the acceptor component on the net dipole moment of the molecule is a strong contributor to the significant differences in the self-assembly of the BT- and PT-based compounds. As electrostatic interactions are an important driving force for self-assembly, it is reasonable that the large change of the local dipole moment resulting from the broad distribution of conformers frustrates the self-assembly process of the BT-containing compound. On the other hand, the PT-based compounds, which may also benefit from extra stability imparted by the pyridyl N-atom, have less variations of the net dipole moment that may enhance/drive self-assembly in the solid state.

As small-molecule BHJ solar cells continue to improve at a rapid pace, so does the need to understand of the link between structure and function. The results presented here suggest the conformational and electrostatic disorder are important factors in the design of new, high-performance small-molecule materials: one must consider not only the nature of the electronic structure and solubilizing alkyl side chains but also more subtle interactions affecting the self-assembly in the solid state. With their facile synthesis and high purity, small-molecule donor materials will continue to be an exciting area of research.

■ ASSOCIATED CONTENT

Ⓢ Supporting Information

Methods and materials, synthesis and spectroscopic characterization of **4**; ^1H and ^{13}C NMR spectra, CV plots, and DSC plots of **4**; absorption spectra of all compounds in the solid state as a function of annealing temperature; UPS plots, charge carrier mobility, XRD plots; and IPCE spectra of **1**−**4**; solar cell data of **1** with PCE = 7.03%; absorption spectra of small-molecule:$PC_{70}BM$ blends with varying DIO concentration; HR-TEM measurements; and table of CV data and frontier molecular orbital energy levels of **1**−**4**. This material is available free of charge via the Internet at http://pubs.acs.org.

■ AUTHOR INFORMATION

Corresponding Author

bazan@chem.ucsb.edu; ajhe@physics.ucsb.edu

Author Contributions

#C.J.T., Y.S., G.C.W., and L.A.P. contributed equally to this work.

Notes

The authors declare no competing financial interest.

■ ACKNOWLEDGMENTS

The TEM characterization was supported by the National Science Foundation (NSF-DMR 0856060). We thank the Office of Naval Research for support of the GIWAX measurements, the Center for Energy Efficient Materials, an Energy Frontier Research Center funded by the Office of Basic Energy Sciences of the U.S. Department of Energy (DE-DC0001009) for supporting the synthesis of the materials used

in this work. Solar cell fabrication and optimization were supported by the Air Force Office of Scientific Research (FA9550-11-1-0063). A portion of this work was done in the UCSB nanofabrication facility, part of the NSF-funded NNIN network. This work made use of MRL Central Facilities supported by the MRSEC Program of the National Science Foundation under Award No. DMR05-20415. The authors acknowledge Dr. Jonathan D. Yuen for supplying the SiO_2/Si substrates with pre-patterned electrodes. C.J.T. acknowledges Stephan Kraemer, Jacek J. Jasieniak, Edward J. Kramer, and Michael L. Chabinyc for useful discussions. L.A.P. acknowledges support from the ConvEne IGERT Program (NSF-DGE 0801627) and a Graduate Research Fellowship from the National Science Foundation (GRFP). Portions of this research were carried out at the Stanford Synchrotron Radiation Lightsource user facility operated by Stanford University on behalf of the U.S. Department of Energy, Office of Basic Energy Sciences. We acknowledge support from the Center for Scientific Computing at the CNSI and MRL: NSF MRSEC (DMR-1121053) and NSF CNS-0960316.

■ REFERENCES

(1) Cheng, Y.-J.; Yang, S.-H.; Hsu, C.-S. *Chem. Rev.* **2009**, *109*, 5868.
(2) Günes, S.; Neugebauer, H.; Sariciftci, N. S. *Chem. Rev.* **2007**, *107*, 1324.
(3) Chen, J.; Cao, Y. *Acc. Chem. Res.* **2009**, *42*, 1709.
(4) Li, C.; Liu, M.; Pschirer, N. G.; Baumgarten, M.; Müllen, K. *Chem. Rev.* **2010**, *110*, 6817.
(5) Chen, L.-M.; Hong, Z.; Li, G.; Yang, Y. *Adv. Mater.* **2009**, *21*, 1434.
(6) Brabec, C. J.; Gowrisanker, S.; Halls, J. J. M.; Laird, D.; Jia, S.; Williams, S. P. *Adv. Mater.* **2010**, *22*, 3839.
(7) Beaujuge, P. M.; Fréchet, J. M. J. *J. Am. Chem. Soc.* **2011**, *133*, 20009.
(8) Inganäs, O.; Zhang, F.; Tvingstedt, K.; Andersson, L. M.; Hellström, S.; Andersson, M. R. *Adv. Mater.* **2010**, *22*, E100.
(9) Servaites, J. D.; Ratner, M. A.; Marks, T. J. *Energ. Environ. Sci.* **2011**, *4*, 4410.
(10) Scharber, M. C.; Mühlbacher, D.; Koppe, M.; Denk, P.; Waldauf, C.; Heeger, A. J.; Brabec, C. J. *Adv. Mater.* **2006**, *18*, 789.
(11) Blom, P. W. M.; Mihailetchi, V. D.; Koster, L. J. A.; Markov, D. E. *Adv. Mater.* **2007**, *19*, 1551.
(12) Boudreault, P.-L. T.; Najari, A.; Leclerc, M. *Chem. Mater.* **2010**, *23*, 456.
(13) Brabec, C. J.; Durrant, J. R. *MRS Bull.* **2008**, *33*, 670.
(14) Krebs, F. C.; Gevorgyan, S. A.; Alstrup, J. *J. Mater. Chem.* **2009**, *19*, 5442.
(15) Dennler, G.; Scharber, M. C.; Brabec, C. J. *Adv. Mater.* **2009**, *21*, 1323.
(16) Price, S. C.; Stuart, A. C.; Yang, L.; Zhou, H.; You, W. *J. Am. Chem. Soc.* **2011**, *133*, 4625.
(17) Chu, T.-Y.; Lu, J.; Beaupré, S.; Zhang, Y.; Pouliot, J.-R. m.; Wakim, S.; Zhou, J.; Leclerc, M.; Li, Z.; Ding, J.; Tao, Y. *J. Am. Chem. Soc.* **2011**, *133*, 4250.
(18) Gong, X.; Tong, M.; Brunetti, F. G.; Seo, J.; Sun, Y.; Moses, D.; Wudl, F.; Heeger, A. J. *Adv. Mater.* **2011**, *23*, 2272.
(19) Holcombe, T. W.; Woo, C. H.; Kavulak, D. F. J.; Thompson, B. C.; Fréchet, J. M. J. *J. Am. Chem. Soc.* **2009**, *131*, 14160.
(20) Liang, Y.; Xu, Z.; Xia, J.; Tsai, S.-T.; Wu, Y.; Li, G.; Ray, C.; Yu, L. *Adv. Mater.* **2010**, *22*, E135.
(21) Wang, E.; Ma, Z.; Zhang, Z.; Vandewal, K.; Henriksson, P.; Inganäs, O.; Zhang, F.; Andersson, M. R. *J. Am. Chem. Soc.* **2011**, *133*, 14244.
(22) Geens, W.; Aernouts, T.; Poortmans, J.; Hadziioannou, G. *Thin Solid Films* **2002**, *403*−*404*, 438.
(23) Peumans, P.; Uchida, S.; Forrest, S. R. *Nature* **2003**, *425*, 158.
(24) Lin, Y.; Li, Y.; Zhan, X. *Chem. Soc. Rev.* **2012**, *41*, 4245.
(25) He, Z.; Zhong, C.; Huang, X.; Wong, W.-Y.; Wu, H.; Chen, L.; Su, S.; Cao, Y. *Adv. Mater.* **2011**, *23*, 4636.
(26) Service, R. F. *Science* **2011**, *332*, 293.
(27) Dou, L.; You, J.; Yang, J.; Chen, C.-C.; He, Y.; Murase, S.; Moriarty, T.; Emery, K.; Li, G.; Yang, Y. *Nat. Photon.* **2012**, *6*, 180.
(28) Small, C. E.; Chen, S.; Subbiah, J.; Amb, C. M.; Tsang, S.-W.; Lai, T.-H.; Reynolds, J. R.; So, F. *Nat. Photon.* **2012**, *6*, 115.
(29) Li, G.; Zhu, R.; Yang, Y. *Nat. Photon.* **2012**, *6*, 153.
(30) Chiu, S.-W.; Lin, L.-Y.; Lin, H.-W.; Chen, Y.-H.; Huang, Z.-Y.; Lin, Y.-T.; Lin, F.; Liu, Y.-H.; Wong, K.-T. *Chem. Commun.* **2012**, *48*, 1857.
(31) Steinmann, V.; Kronenberg, N. M.; Lenze, M. R.; Graf, S. M.; Hertel, D.; Meerholz, K.; Bürckstümmer, H.; Tulyakova, E. V.; Würthner, F. *Adv. Energ. Mater.* **2011**, *1*, 888.
(32) http://www.heliatek.com
(33) Lee, O. P.; Yiu, A. T.; Beaujuge, P. M.; Woo, C. H.; Holcombe, T. W.; Millstone, J. E.; Douglas, J. D.; Chen, M. S.; Fréchet, J. M. J. *Adv. Mater.* **2011**, *23*, 5359.
(34) Ko, H. M.; Choi, H.; Paek, S.; Kim, K.; Song, K.; Lee, J. K.; Ko, J. *J. Mater. Chem.* **2011**, *21*, 7248.
(35) Mayerhöffer, U.; Deing, K.; Gruß, K.; Braunschweig, H.; Meerholz, K.; Würthner, F. *Angew. Chem., Int. Ed.* **2009**, *48*, 8776.
(36) Bagnis, D.; Beverina, L.; Huang, H.; Silvestri, F.; Yao, Y.; Yan, H.; Pagani, G. A.; Marks, T. J.; Facchetti, A. *J. Am. Chem. Soc.* **2010**, *132*, 4074.
(37) Shang, H.; Fan, H.; Liu, Y.; Hu, W.; Li, Y.; Zhan, X. *Adv. Mater.* **2011**, *23*, 1554.
(38) Walker, B.; Tamayo, A. B.; Dang, X.-D.; Zalar, P.; Seo, J. H.; Garcia, A.; Tantiwiwat, M.; Nguyen, T.-Q. *Adv. Funct. Mater.* **2009**, *19*, 3063.
(39) Loser, S.; Bruns, C. J.; Miyauchi, H.; Ortiz, R. o. P.; Facchetti, A.; Stupp, S. I.; Marks, T. J. *J. Am. Chem. Soc.* **2011**, *133*, 8142.
(40) Wei, G.; Wang, S.; Sun, K.; Thompson, M. E.; Forrest, S. R. *Adv. Energ. Mater.* **2011**, *1*, 184.
(41) Wei, G.; Xiao, X.; Wang, S.; Sun, K.; Bergemann, K. J.; Thompson, M. E.; Forrest, S. R. *ACS Nano* **2011**, *6*, 972.
(42) Walker, B.; Tamayo, A.; Duong, D. T.; Dang, X.-D.; Kim, C.; Granstrom, J.; Nguyen, T.-Q. *Adv. Energ. Mater.* **2011**, *1*, 221.
(43) Li, Y.; Guo, Q.; Li, Z.; Pei, J.; Tian, W. *Energ. Environ. Sci.* **2010**, *3*, 1427.
(44) Roncali, J. *Acc. Chem. Res.* **2009**, *42*, 1719.
(45) Mishra, A.; Bäuerle, P. *Angew. Chem., Int. Ed.* **2012**, *51*, 2020.
(46) Bundgaard, E.; Hagemann, O.; Manceau, M.; Jørgensen, M.; Krebs, F. C. *Macromolecules* **2010**, *43*, 8115.
(47) Li, Z.; He, G.; Wan, X.; Liu, Y.; Zhou, J.; Long, G.; Zuo, Y.; Zhang, M.; Chen, Y. *Adv. Energ. Mater.* **2012**, *2*, 74.
(48) Sun, Y.; Welch, G. C.; Leong, W. L.; Takacs, C. J.; Bazan, G. C.; Heeger, A. J. *Nat. Mater.* **2012**, *11*, 44.
(49) Würthner, F.; Meerholz, K. *Chem*−*Eur. J.* **2010**, *16*, 9366.
(50) Fitzner, R.; Elschner, C.; Weil, M.; Uhrich, C.; Körner, C.; Riede, M.; Leo, K.; Pfeiffer, M.; Reinold, E.; Mena-Osteritz, E.; Bäuerle, P. *Adv. Mater.* **2012**, *24*, 675.
(51) Henson, Z. B.; Welch, G. C.; van der Poll, T.; Bazan, G. C. *J. Am. Chem. Soc.* **2012**, *134*, 3766.
(52) Welch, G. C.; Perez, L. A.; Hoven, C. V.; Zhang, Y.; Dang, X.-D.; Sharenko, A.; Toney, M. F.; Kramer, E. J.; Nguyen, T.-Q.; Bazan, G. C. *J. Mater. Chem.* **2011**, *21*, 12700.
(53) Welch, G. C.; Bazan, G. C. *J. Am. Chem. Soc.* **2011**, *133*, 4632.
(54) Steinberger, S.; Mishra, A.; Reinold, E.; Levichkov, J.; Uhrich, C.; Pfeiffer, M.; Bauerle, P. *Chem. Commun.* **2011**, *47*, 1982.
(55) Zhou, H.; Yang, L.; Price, S. C.; Knight, K. J.; You, W. *Angew. Chem., Int. Ed.* **2010**, *49*, 7992.
(56) Blouin, N.; Michaud, A.; Gendron, D.; Wakim, S.; Blair, E.; Neagu-Plesu, R.; Belletête, M.; Durocher, G.; Tao, Y.; Leclerc, M. *J. Am. Chem. Soc.* **2007**, *130*, 732.
(57) Mei, J.; Graham, K. R.; Stalder, R.; Reynolds, J. R. *Org. Lett.* **2010**, *12*, 660.
(58) Yun, S. W.; Kim, J. H.; Shin, S.; Yang, H.; An, B.-K.; Yang, L.; Park, S. Y. *Adv. Mater.* **2012**, *24*, 911.

(59) Sun, Y.; Takacs, C. J.; Cowan, S. R.; Seo, J. H.; Gong, X.; Roy, A.; Heeger, A. J. *Adv. Mater.* **2011**, *23*, 2226.
(60) Rogers, J. T.; Schmidt, K.; Toney, M. F.; Kramer, E. J.; Bazan, G. C. *Adv. Mater.* **2011**, *23*, 2284.
(61) Mayer, A. C.; Toney, M. F.; Scully, S. R.; Rivnay, J.; Brabec, C. J.; Scharber, M.; Koppe, M.; Heeney, M.; McCulloch, I.; McGehee, M. D. *Adv. Funct. Mater.* **2009**, *19*, 1173.
(62) Chabinyc, M. L. *Polym. Rev.* **2008**, *48*, 463.
(63) Lovinger, A. J.; Katz, H. E.; Dodabalapur, A. *Chem. Mater.* **1998**, *10*, 3275.
(64) Drummy, L. F.; Davis, R. J.; Moore, D. L.; Durstock, M.; Vaia, R. A.; Hsu, J. W. P. *Chem. Mater.* **2010**, *23*, 907.
(65) Hammond, M. R.; Kline, R. J.; Herzing, A. A.; Richter, L. J.; Germack, D. S.; Ro, H.-W.; Soles, C. L.; Fischer, D. A.; Xu, T.; Yu, L.; Toney, M. F.; DeLongchamp, D. M. *ACS Nano* **2011**, *5*, 8248.
(66) Wei, G.; Lunt, R. R.; Sun, K.; Wang, S.; Thompson, M. E.; Forrest, S. R. *Nano Lett.* **2010**, *10*, 3555.
(67) Zhang, X.; Hudson, S. D.; DeLongchamp, D. M.; Gundlach, D. J.; Heeney, M.; McCulloch, I. *Adv. Funct. Mater.* **2010**, *20*, 4098.
(68) Collins, B. A.; Cochran, J. E.; Yan, H.; Gann, E.; Hub, C.; Fink, R.; Wang, C.; Schuettfort, T.; McNeill, C. R.; Chabinyc, M. L.; Ade, H. *Nat. Mater.* **2012**, *11*, 536.
(69) Ros, M. B.; Serrano, J. L.; de la Fuente, M. R.; Folcia, C. L. *J. Mater. Chem.* **2005**, *15*, 5093.
(70) Patnaik, S. S.; Plimpton, S. J.; Pachter, R.; Adams, W. W. *Liq. Cryst.* **1995**, *19*, 213.
(71) Patnaik, S. S.; Pachter, R.; Bunning, T. J.; Crane, R. L.; Adams, W. W. *Liq. Cryst.* **1994**, *16*, 911.
(72) Patnaik, S. S.; Lupo, J. A.; Pachter, R. *Comput. Theor. Poly. Sci.* **1998**, *8*, 39.
(73) Huang, H.; Chen, Z.; Ortiz, R. P.; Newman, C.; Usta, H.; Lou, S.; Youn, J.; Noh, Y.; Baeg, K.; Chen, L. X.; Facchetti, A.; Marks, T. *J. Am. Chem. Soc.* **2012**, *134*, 10966.